Engineering Structures 306 (2024) 117877

Contents lists available at ScienceDirect

Engineering Structures

journal homepage: www.elsevier.com/locate/engstruct

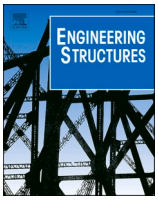

Experimental and numerical study of G-HPC slabs rapidly repaired by G-HPC canvas and G-UHPC under contact detonations

Shenchun Xu [a], Hao Zeng [a], Pengcheng Yuan [a,*], Jian Liu [a], Ting Yang [a], Ruizhe Shao [b], Yu Su [c], Chengqing Wu [b,*]

[a] Earthquake Engineering Research & Test Center, Guangzhou University, Guangzhou 510006, China
[b] School of Civil and Environmental Engineering, University of Technology Sydney, NSW 2007, Australia
[c] RockTek Co. Ltd., Daye 435100, China

ARTICLE INFO

Keywords:
Concrete slab
Contact blast-resistant performance
Novel G-HPC canvas
G-UHPC
Rapidly repair
Numerical simulations

ABSTRACT

The rapid repair of engineering structures damaged due to explosions can enhance the structural impact resistance after an explosion, thereby reducing the potential for casualties and property losses. A novel concrete canvas was firstly proposed based on G-HPC (geopolymer-based high performance concrete), UHMWPEWF (ultra-high molecular weight polyethylene woven fabric), and 3D BFG (basalt fiber grid) to rapidly repair engineering structures and render their blast resistance. A sequence of contact blast tests was systematically conducted to verify the feasibility of the proposed G-HPC canvas. A normal reinforced concrete slab and a steel-wire mesh (SWM) reinforced G-HPC slab were initially damaged by the contact blast loading, afterwards, the damaged concrete slabs were rapidly repaired by G-UHPC (geopolymer-based ultra-high-performance concrete) and the novel G-HPC canvas. The rapidly repaired concrete slabs were subsequently tested by contact blast loading. A precise 3D finite element model was then developed and calibrated based on the experimental results. Eventually, numerical simulations were performed to better understand the contribution of main parameters including repair materials filling the internal slab, steel-wire mesh, G-HPC canvas location and its thickness towards the improvement of the rapidly repaired slabs against the contact blast loading. The experimental and numerical results indicated that the SWM reinforced G-HPC slab has superior blast-resistance compared with the RC slab and the proposed method to rapidly repair the damaged slabs was feasible. The G-HPC canvas should be placed properly since the location of the G-HPC canvas is related to whether fragments are produced on the rear surface of the damaged slab. Increasing the G-HPC canvas thickness and the layers of SWM could significantly reduce the damage area of the repaired slab.

1. Introduction

In recent decades, bomb terrorists and accidental explosions still occur frequently around the world [1]. Engineering structures are facing an increasingly severe threat of explosion disasters. The blast load would directly result in damage to engineering structures and injuries to people surrounding the explosion source. The high-velocity splattering of fragments generated from the damaged structures would further aggravate the explosion catastrophes and induce secondary disasters. Thus, the safety of engineering structures under blast loading has been a focus of engineers and scholars.

Enhancing the blast resistance of engineering structures fundamentally relies on the amelioration of construction material mechanical properties [2–4]. Among them, PC-UHPC (Portland cement-based ultra-high-performance concrete) is regarded as a very potential construction material in protective structures against intense dynamic loading, and the superior blast resistance of PC-UHPC members has been proven by an extensive body of investigative research [5–9]. However, 800–1100 kg Portland cement would be consumed in the manufacture of PC-UHPC in 1 m^3, which is 3-fold higher than the conventional concrete [10]. Besides, the application of superplasticizers is a common practice in the production of PC-UHPC, aiming to enhance workability while maintaining a minimal water-to-binder ratio. Therefore, the large-scale use of PC-UHPC in protective structures would consume more energy and resources, and generate a pronounced adverse influence on the natural environment [11]. To overcome these shortcomings, a novel

* Corresponding authors.
E-mail addresses: pengcheng.yuan@gzhu.edu.cn (P. Yuan), chengqing.wu@uts.edu.au (C. Wu).

https://doi.org/10.1016/j.engstruct.2024.117877
Received 11 October 2023; Received in revised form 19 February 2024; Accepted 15 March 2024
Available online 19 March 2024

type of UHPC based on geopolymer technology, denoted as G-UHPC, has been developed in recent years. Owing to no Portland cement being used in G-UHPC, it was regarded as a green construction material while its mechanical properties were proved to be comparable to PC-UHPC [12–15]. The hardening time of G-UHPC can also be adjusted based on the mixture design [10]. Therefore, G-UHPC is of remarkable potential in the rapid construction or repair of protective structures, which is critical for the safety of important targets, especially in the military field.

In terms of structural rapid repair, the extensive adoption of innovative materials and technologies broadens the spectrum of options available to engineers. This encompasses fiber reinforced polymers (FRP), polymer-modified concrete (PMC), and among others [16–18]. This diversity fosters a more efficient approach to the repair and fortification of impaired structures. Nevertheless, it is crucial to recognize that each material and technology comes with its unique set of merits and drawbacks. FRP composites present notable advantages, including lightweight design, high strength, and corrosion resistance. Their common application has been found in the rapid repair and strengthening of beams, columns, and other structural elements [19–21], showcasing exceptional tensile strength. However, these materials also exhibit certain drawbacks, such as elevated costs, thermal expansion coefficient mismatching with concrete, and susceptibility to aging at adhesive joints. Conversely, PMC achieves impressive strength within a relatively short period, offering distinct benefits for prompt structural repair [22]. However, there are also potential drawbacks, such as poor flowability and possible issues with long-term strength and durability. Concrete canvas has been used in civil and military engineering as a relatively new technology since it can be in service in less than 3 days after spraying [23,24]. As a 3D fabric-reinforced cement-based composite, it could be fabricated by filling the 3D fabric with cement or cement-based composite powder [25–28]. Such a canvas has the advantages of mechanical properties, durable, waterproof, fire resistance, and controllable thickness. Thus, it would be a beneficial trial for combining G-UHPC and concrete canvas to rapidly repair the damaged RC members under blast loading.

Currently, investigations on the blast resistance of G-UHPC elements have been reported and fruitful results have been achieved [29,30]. However, the blast resistance of the damaged concrete element rapidly repaired by G-UHPC and the concrete canvas was still limitedly explored. Therefore, the feasibility of the adoption of SWM and G-HPC in pursuit of enhancing the blast-resistance of the RC slab was first verified by the contact blast test in this study. Subsequently, a novel concrete canvas (G-HPC canvas) fabricated by G-HPC, UHMWPEWF, and 3D BFG was developed. On this basis, a method based on G-HPC canvas and G-UHPC was proposed to rapidly repair the damaged slab induced by the first blast. The rapidly repaired specimens were also explored by the subsequent contact blast tests. Finally, a 3D refined finite element model was established and validated. The failure mechanism was revealed by the FE model and the effect of the steel-wire mesh, repair materials, G-HPC canvas location and thickness on the blast resistance of rapidly repaired specimens was also explored by numerical simulations. The results achieved in this study would additionally advance the utilization of G-UHPC and concrete canvas within the field of protective engineering and provide design references for this type of composite structure against blast loading.

2. Design of novel G-HPC canvas

The novel G-HPC canvas proposed includes G-HPC, UHMWPEWF, and 3D BFG, as illustrated in Fig. 1. When fabricated, the UHMWPEWF was firstly unrolled followed by positioning the 3D BFG on it. Afterwards, the G-HPC in the form of dry powder should be evenly sprinkled until the 3D BFG is completely filled. Eventually, the UHMWPEWF should be rolled to fully cover the 3D BFG and the G-HPC dry powder. In this study, the thickness of the G-HPC canvas is 10.24 mm including 10 mm thickness of the 3D BFG and 0.24 mm thickness of two layers of the UHMWPEWF. The mechanical properties of UHMWPE (ultra-high molecular weight polyethylene) and basalt fiber are listed in Table 1. When used, the target should be covered by the canvas followed by sprinkling water and naturally cured until the test day. The specific hydration of G-HPC can be found in the literature [10]. Compared with conventional concrete canvas, the G-HPC canvas can be in service in 1 day after sprinkling water as the compressive strength of G-HPC would reach 40 MPa at this time. The proposed rapid repair method holds significant importance, as its uniqueness lies in its swift implementation, enabling a prompt response to emergency situations while minimizing downtime in structural maintenance. Simultaneously, it plays a crucial role in enhancing the overall structural resilience against external loads. This feature makes the repair method particularly valuable in emergency scenarios or situations requiring rapid reinforcement of structures to ensure overall safety.

Table 1
Mechanical properties of UHMWPE and BF.

Materials	Diameter (μm)	Density (g/cm^3)	Tensile strength (MPa)	Young's modulus (GPa)	Elongation (%)
UHMWPE	50	0.97	3200	130	4.0
BF	10	2.64	3000	100	2.5

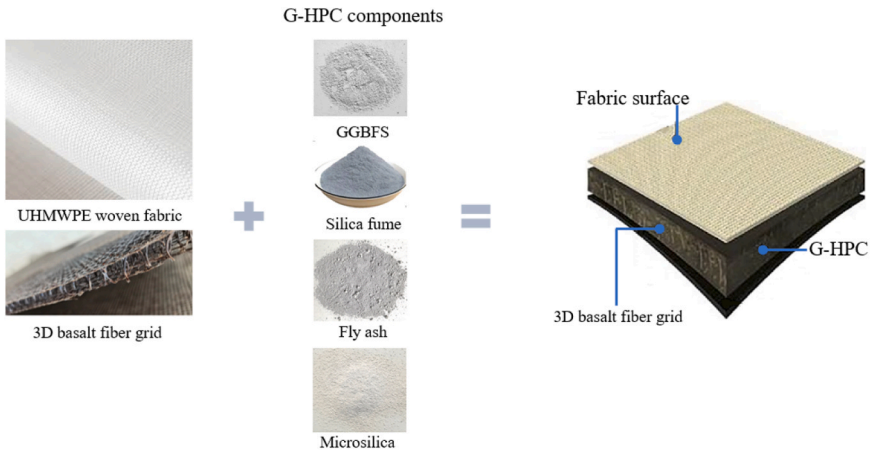

Fig. 1. Details of G-HPC canvas.

3. Design and fabrication of specimens

Firstly, two slabs, including an HRB 400 steel rebar reinforced conventional C40 slab and 20 layers of SWMs reinforced G-HPC slab, were devised to explore the efficacy of the G-HPC and SWMs in improving the blast resistance of RC structures. Subsequently, the damaged slabs after contact explosions were rapidly repaired by G-UHPC and G-HPC canvas to substantiate the viability of the proposed rapid repair method against contact explosions. As illustrated in Fig. 2(a), the same dimensions 1500 × 1500 × 200 mm were employed for all specimens.

Fig. 2(b) exhibits the construction of the conventional C40 slab reinforced by HRB 400 steel rebars. Based on GB 50010–2010 [31], a 2% reinforcement ratio was adopted for this slab, consequently, the dimensions of the steel rebars were specified as 16 mm in diameter with a

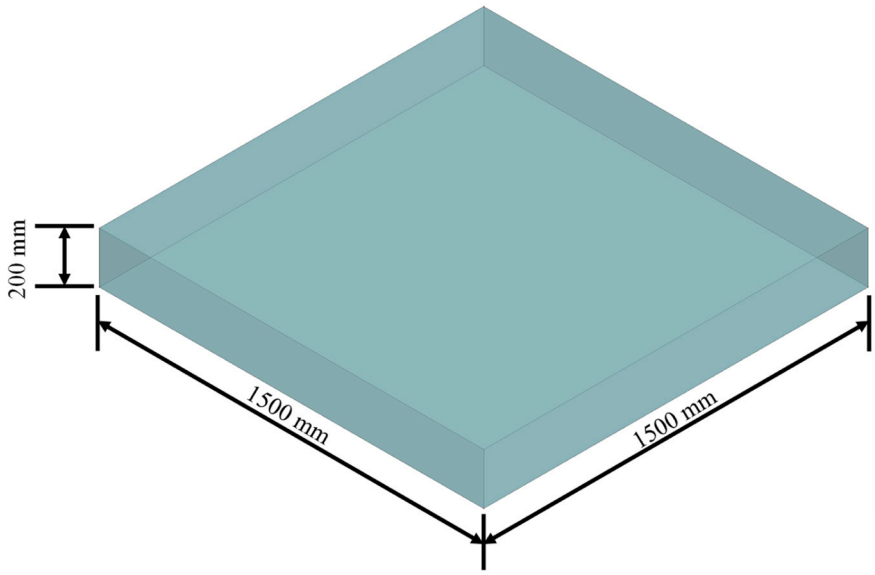

(a) The plan view of the slabs

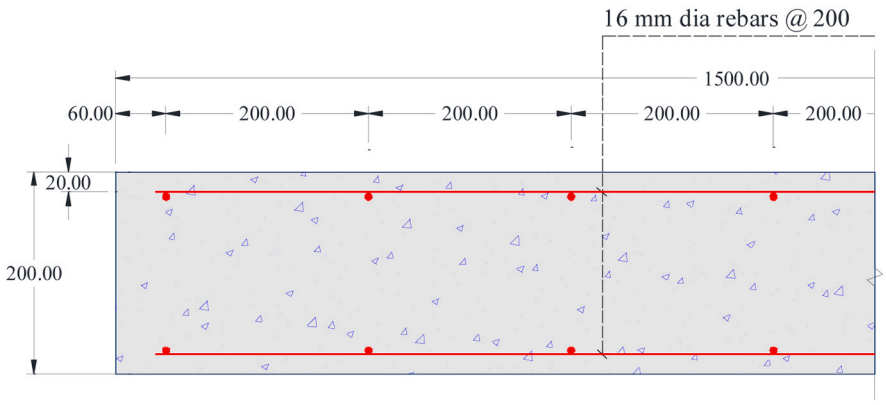

(b) The layout of the RC specimen

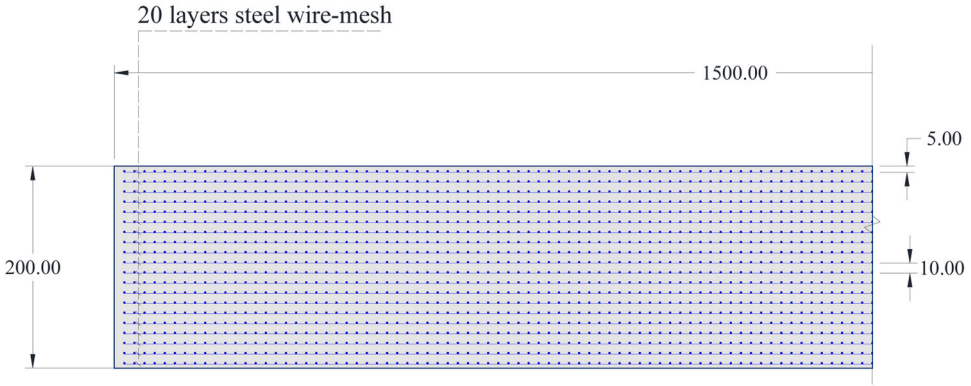

(c) The layout of the 20 SWMs- G-HPC specimen

Fig. 2. The details of the specimens.

(a) Installed steel-wire meshes (b) Pouring of G-HPC

Fig. 3. The fabrication process of SWMs reinforced G-HPC slab.

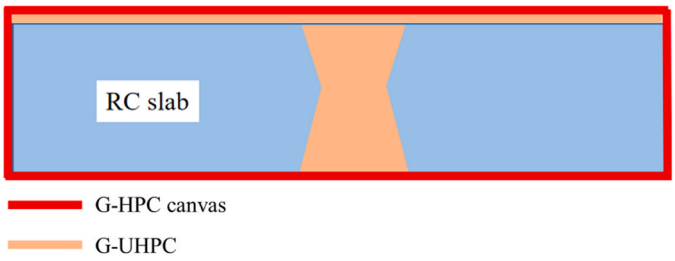

Fig. 5. Diagram of construction of repaired RC slab.

spacing of 200 mm. Additionally, the thickness of the protective cover was 20 mm. The details of the 20 layers of SWMs reinforced G-HPC slab with a 1.57% reinforcement ratio is shown in Fig. 2(c). As indicated, the spacing between SWMs layer was 10 mm.

Fig. 3 shows the process of manufacturing the SWMs reinforced G-HPC slab. Twenty layers of SWMs were initially positioned within the preassembled formwork, meticulously layering them with predetermined intervals (Fig. 3(a)). Subsequently, the specimen was produced by introducing G-HPC into the formwork (Fig. 3(b)). After prefabrication, maintain it at room temperature for 24 h, and then subject it to rigorous curing at an elevated temperature of 90 ± 5 °C for a duration of 48 h.

The repair strategy involves pouring high-strength 1.5% steel fiber reinforced G-UHPC at the damaged areas of the slab (craters and spalling) to maintain structural integrity and enhance overall blast resistance. Incorporating a layer of 1.5% steel fiber-reinforced G-UHPC on the surface further enhances the bonding performance between the damaged slab and the G-HPC canvas. Finally, covering the slab with the G-HPC canvas provides an additional protective layer, reinforcing the resilience of the repaired slab and acting as a barrier against external impacts. In the repair process, as illustrated in Fig. 4 using the conventional RC slab as an example. Fig. 4(a) emphasizes the initial cleaning of the damaged slab to ensure reliable bonding with the G-HPC canvas. Subsequently, spread the G-HPC canvas with dimensions of 3650 × 1250 × 10.24 mm on the ground and sprinkle it with water (Fig. 4(b)). Then, lift the RC slab to the predetermined position on the G-HPC canvas, and pour 1.5% steel fiber reinforced G-UHPC with superior mechanical properties (compressive strength > 160 MPa) into the hole resulting from the contact detonation (Fig. 4(c)). After that, the upper surface of the RC slab should be covered by a layer of 1.5% steel fiber reinforced G-UHPC with a thickness of 5 mm to further improve the bonding behavior between the damaged slab and the G-HPC canvas. Eventually, the specimen repaired by the hardened G-UHPC was wrapped by the concrete canvas to finish the rapid repair process (Fig. 4(d)). After 24 h following the completion of the repair process, a second contact detonation is conducted to study the blast resistance of the rapidly repaired slab. Fig. 5 exhibits the diagram of the eventual construction of the repaired RC slab.

4. Materials

Ground granulated blast furnace slag (GGBFS), Class F fly ash, and silica fume are the binder material of the G-HPC. Furthermore, the microstructure and the flowability of G-HPC can be improved by adding the fly ash and silica fume as supplementary binder materials due to their micron-sized spherical particles. The alkaline activator used to excite the above binder materials was manually fabricated by mixing NaOH and waterglass solution. The purity of NaOH is 98 ± 1% and the concentration of waterglass solution is 35%. The industrial-grade sodium silicate in 3 modulus and water were used to produce the waterglass solution. The quartz sand served as the fine aggregates and no coarse aggregates were added in this study. Table 2 shows the mixture design of G-HPC. Correspondingly, Table 3 (wt%) lists the chemical compositions of GGBFS, Class F fly ash, and silica fume, in which LoI

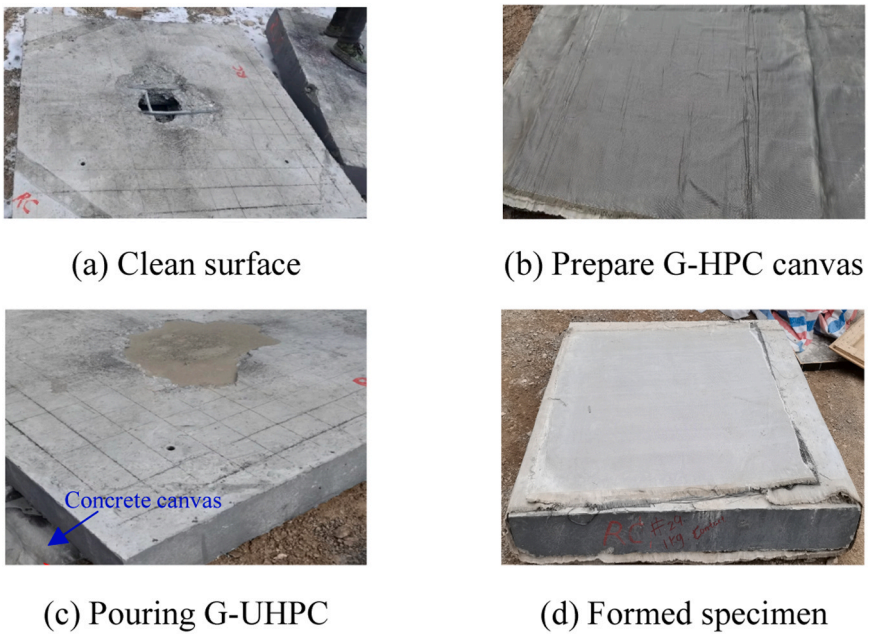

(a) Clean surface (b) Prepare G-HPC canvas

(c) Pouring G-UHPC (d) Formed specimen

Fig. 4. Repair process of damaged slab.

Table 2
The proportion of each component in the G-HPC mixture (wt%).

GGBFS	Silica fume	Fly ash	Sand 1	Sand 2	NaOH	Waterglass	Water
1.000	0.100	0.160	0.602	0.458	0.0743	0.312	0.384

Note: In this table, GGBS refers to Granulated Blast-Furnace Slag; the particle size of Sand1 ranges from 5.2 μm to 0.212 mm, and that of Sand2 lies in the range of 0.212 mm to 0.83 mm.

Table 3
The chemical composite of the granulated blast furnace slag, Class F fly ash, and silica fume (wt%).

	CaO	SiO_2	Al_2O_3	MgO	K_2O	Fe_2O_3	Na_2O	SO_3	Others	LOI
GGBS	43.739	25.318	13.076	7.539	0.343	0.362	0.401	2.373	6.485	1.40
Fly ash	11.02	52.87	22.14	4.23	2.90	4.23	0.96	0.08	2.05	1.24
Silica fume	0.3	94.7	1.2	0.7	0.9	0.9	1.3	-	-	3.45

refers to the loss on ignition at 1000 ℃. Furthermore, straight smooth steel fibers with dimensions of 0.12 mm in diameter and 10 mm in length were added into the mixture of G-HPC to produce G-UHPC and the volumetric ratio was 1.5%.

The average compressive strength of six cubic specimens in the dimensions of 100 mm × 100 mm × 100 mm was regarded as the final compressive strength of G-HPC or G-UHPC. Fig. 6 shows the stress-strain relationships of G-HPC and G-UHPC, indicating that the compressive strengths of G-HPC and G-UHPC were 84.5 and 172.2 MPa, respectively. Besides, the toughness of G-UHPC (the area under the stress-strain relationship) was also much superior to G-HPC. It is worth noting that, for simplification, only averaged values of three samples for each type are shown in Fig. 6.

Twenty layers of SWMs were used to enhance the mechanical properties of G-HPC, especially for the toughness. The diameter of the steel wire is approximately 1 mm and the mesh spacing was 10 mm, as shown in Fig. 7. The mechanical properties of the SMWs and HRB 400 steel rebars are listed in Table 4.

5. Contact-explosion tests

5.1. Experimental setup

The setup of field contact blast tests is shown in Fig. 8. The support consists of four concrete pillars and a square steel frame (formed by welding four U steel channels). The concrete pillars were fixed on the ground and the steel frame was positioned on the top of the concrete pillars. Five rectangular charges, each weighing 0.2 kg and measuring 100 mm × 50 mm × 25 mm in dimensions, were vertically arranged atop the specimen's central surface to constitute the TNT explosive. The initial detonation commenced with the ignition of the uppermost rectangular charge via an electric detonator insertion, subsequently leading to the sequential detonation of the remaining charges. Table 5 presents the test matrix, which indicates that the specimens would initially suffer from contact blast loading with 1 kg TNT detonation. However, the mass of the charge in the second blast was different since the RC slab was more severely damaged in the first blast compared with the SWMs reinforced G-HPC slab.

5.2. Experimental results and discussion

Fig. 9 shows the observations in the tests and Table 6 summarizes the experimental results. As observed, the failure mode is consistent with the classical shock wave theory, i.e., the concrete directly subjected to the contact blast loading was crushed owing to the intense compressive stress generated from the detonation of TNT, and the spalling failure was generated on the rear concrete since the reflected tensile stress exceeded the tensile strength of concrete upon the propagation of the compressive stress wave to the free (rear) surface.

The RC slab presented the breach-perforation failure. The dimensions of the crater observed on the surface facing the charge were 410 mm in diameter and 50 mm in depth. On the bottom, a spalling with a 745 mm diameter and a 150 depth was observed. Thus, the crater and the spalling were connected forming a hole. In this area, the reinforcement was exposed and exhibited obvious deformation. For the specimen, 20SWMs-G-HPC, a crater with a 350 mm diameter and an 80 mm depth was observed on the top surface, whereas a bulge was formed on the bottom surface with a 400 mm diameter and a 100 mm height. Meanwhile, it can be observed that SWMs were fractured in the crater, and a little cover concrete was spalled from the rear surface. By comparing the experimental results of the specimens RC and 20SWMs-G-HPC, it indicated that the utilization of SWMs yielded a noteworthy enhancement on the spalling resistance of the concrete slab, however, it was worth noting that the crater damage was enhanced as the input energy consumed through spalling in the RC slab was now dissipated by the crush of concrete.

After repair, only the crater failure mode resulted from the subsequent contact detonation was observed. For Re-RC, the first layer of fiber fabric was overturned and the keel was exposed. The crater exhibited dimensions measuring 225 mm in diameter and 35 mm in depth. It can be observed that, in comparison with its unrepaired state, the diameter and depth of the crater after repair have decreased by 45% and 30%, respectively. On the rear surface, an inconspicuous bulge was observed. However, the dimensions of the bulge were not recorded due to an incorrect operation. The comparison of the experimental results of RC with Re-RC indicated that the rapid repair method proposed in this study

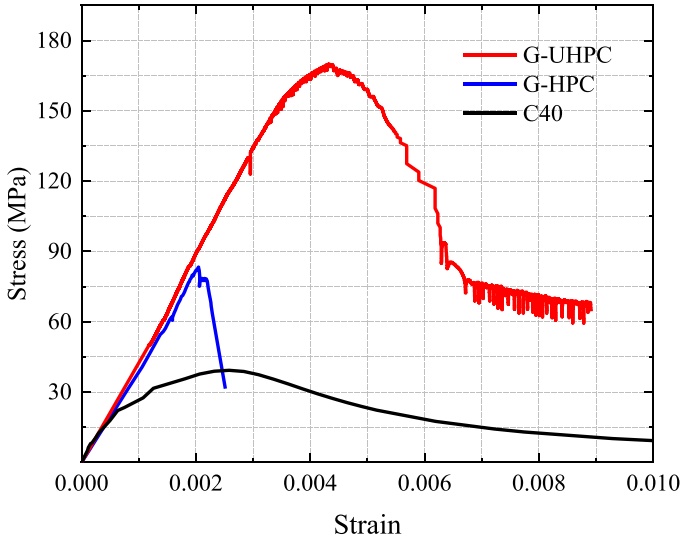

Fig. 6. Stress-strain relationships of G-UHPC, G-HPC and C40 concrete.

has the ability to transit the failure mode to the crater from breach-perforation, i.e., significantly improve the contact blast resistance of RC slab. This is beneficial to the safety of important targets behind protective engineering structures. Especially, it can protect them from the harm of fragments generated from the spalling. A similar observation was presented on the specimen Re-20SWMs-G-HPC, and the dimensions of the crater located on the top surface were recorded as 242.5 mm in diameter and 20 mm in depth, respectively. It can be noted that, as compared to its unrepaired condition, the post-repair crater exhibits a reduction of 30.7% in diameter and 75% in depth. The top layer of fiber fabric was also overturned and the keel was also exposed.

Overall, the utilization of G-HPC and SWM can possess the capacity to markedly augment the capacity of concrete slabs to withstand contact blasts compared with the NSC and steel rebar. The proposed rapid repair method based on G-HPC canvas and G-UHPC is effective in resisting intense blast loading.Table 6 Summary of test and numerical results.

wave and the slabs. Non-reflection boundary was applied on the surface of the ALE dominant to create an infinite space to avoid the effect of the reflected blast wave.

Fig. 11 presents the FE models of the repaired specimens. Besides the original one, it includes the G-HPC canvas and G-UHPC. The G-HPC canvas was simplified as a sandwich structure including two fabrics and a BF-reinforced G-HPC core in the FE model since it would consume a lot of computational resources if the 3D BF (basalt fiber) grid was established in detail. The perfect bonding assumption was adopted for the G-HPC canvas and the damaged slab, thus, no contact algorithm was used in this study to describe the interaction between the G-HPC canvas and the damaged slab.

The numerical simulation on the repaired specimens under the contact blast loading was carry out by the full restart analysis in LS-DYNA. Before restart analysis, the damage indexes of concrete elements suffered from the first contact blast loading were extracted and allocated to the repaired specimen by the keyword INI-

Test					
Specimen codes	Crater diameter (mm)	Crater depth (mm)	Spalling/ Bulge diameter (mm)	Spalling/ Bulge depth (mm)	Failure pattern
RC	410	50	745	150	breach-perforation
20SWMs-G-HPC	350	80	400	100	crater and spalling
Re-RC	225	35	—	—	crater and bulge
Re-20SWMs-G-HPC	242.5	20	—	—	crater and bulge
Numerical simulation					
RC	362	50	680	150	breach-perforation
20SWMs-G-HPC	300	70	360	86	crater and spalling
Re-RC	240	34	—	28	crater and bulge
Re-20SWMs-G-HPC	250	17	—	15	crater and bulge

Note: In this table, "—" means the data was not obtained.

6. Numerical simulation

6.1. Finite element model

Numerical simulations were carried out by the explicit dynamic software LS-DYNA to further explore the failure mechanism of the repaired specimens under contact blast loading and to reveal the effect of main parameters including the repair material filling the damage area, SWMs, G-HPC canvas location and its thickness in detail. The 3D finite element (FE) models for predicting the behavior of RC and 20SWMs-G-HPC under contact blast loading were firstly developed, as shown in Fig. 10. It indicates that both the FE models include air, concrete, TNT, steel frame and supports, while the reinforcements and steel-wire mesh are their main difference. The developed FE model reproduced the test setup well.

The S-ALE (Structured Arbitrary Lagrangian-Eulerian) algorithm embedded in the explicit dynamic software LS-DYNA was used to develop the FE models since it is capable of handling FSI (fluid-structure interaction) problems more effectively, especially when it comes to element erosion. Moreover, this new algorithm would generate structured ALE mesh automatically, thus, listing all the elements and nodes used for ALE mesh in the input deck becomes unnecessary. For larger ALE problems, the input deck size will be greatly reduced. Most importantly, the S-ALE algorithm exhibits higher computational efficiency as compared to the traditional ALE algorithm. More details on the S-ALE algorithm can be found in reference [32]. To show the main parts clearly, the air part is not shown in Fig. 10.

The perfect bonding was assumed between reinforcements/steel-wire meshes and concrete, which was achieved through the constrained-based coupling algorithm defined in CONSTRAINED_ BEAM_IN_SOLID. The interactions between the concrete, steel frame, and the supports were simulated by the surface-to-surface contact algorithm. The penalty function coupling algorithm embedded in ALE_STRUCTURED_FSI was used to perform the interaction between the blast

TIAL_STRESS_SOLID. In this process, a MATLAB program compiled by oneself was used due to the massive elements. Meanwhile, the erosion elements in the first blast event were re-established with new material models. For instance, the erosion elements in the RC slab were re-established, and the K&C material model with a series of parameters describing the mechanical behavior of G-UHPC was endowed to them.

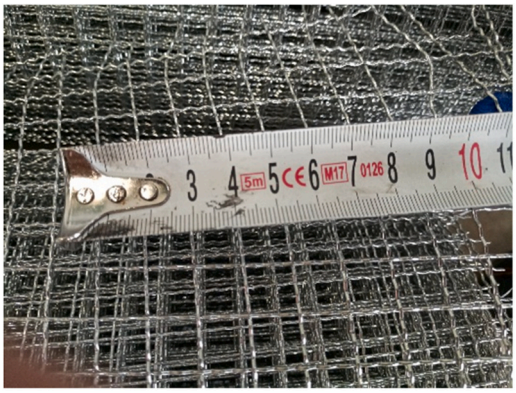

Fig. 7. Details of steel-wire mesh.

Table 4
Properties of SWMs and HRB400 steel rebar.

Materials	Yield strength (MPa)	Tensile strength (MPa)	Young's modulus (GPa)	Elongation percentage (%)
Steel rebar	428.3	615.8	208	20.3
SWM	800	1400	205	28.2

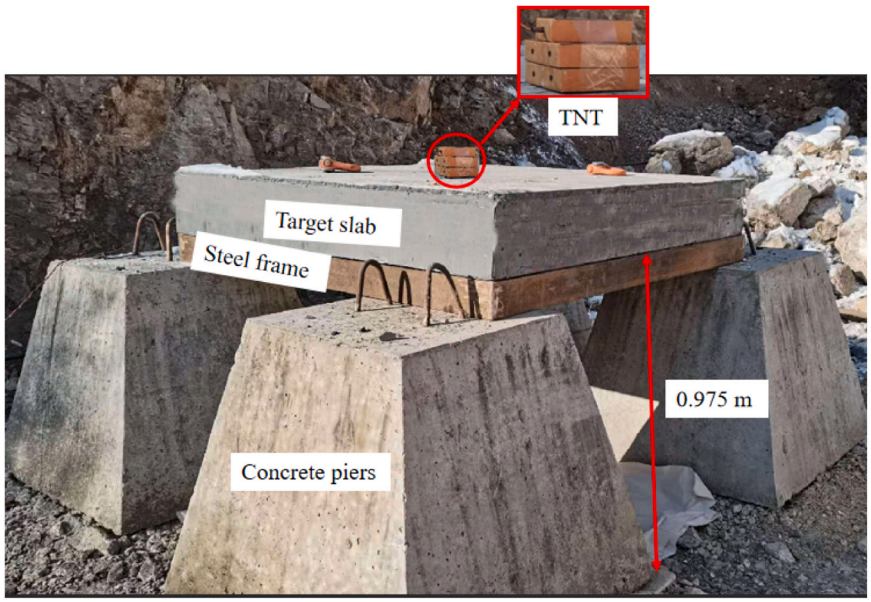

Fig. 8. Setup of field contact blast tests (units: m).

Table 5
The test matrix.

Specimen codes	TNT mass (kg)	Blast event
RC	1.0	contact blast
20SWMs-G-HPC	1.0	
Re-RC	0.6	
Re-20SWMs-G-HPC	1.0	

Note: In this table, the specimens were labeled based on the reinforcement method, matrix material, and repaired or not. For instance, the specimen Re-20SWMs- G-HPC was fabricated by reinforcing G-HPC with 20 layers of SWMs and repaired by G-HPC canvas.

6.2. Material models

6.2.1. Steel material models

The steel frame was regarded as an elastic material (MAT_ELASTIC) for saving computational resources. The kinematic hardening plasticity model (MAT_PLASTIC_KINEMATIC) was exploited to model the mechanical behavior of steel bars and SWMs, and its effectiveness in analyzing the structural performance of RC members under contact blast loading has been verified by a lot of studies [29]. The mechanical properties shown in Table 3, including Young's modulus, yield strength, and ultimate strength, were input in this material model. Besides, the steel materials have significantly different dynamic properties compared with their static behavior, thus, the Cowper-Symonds model of DIF

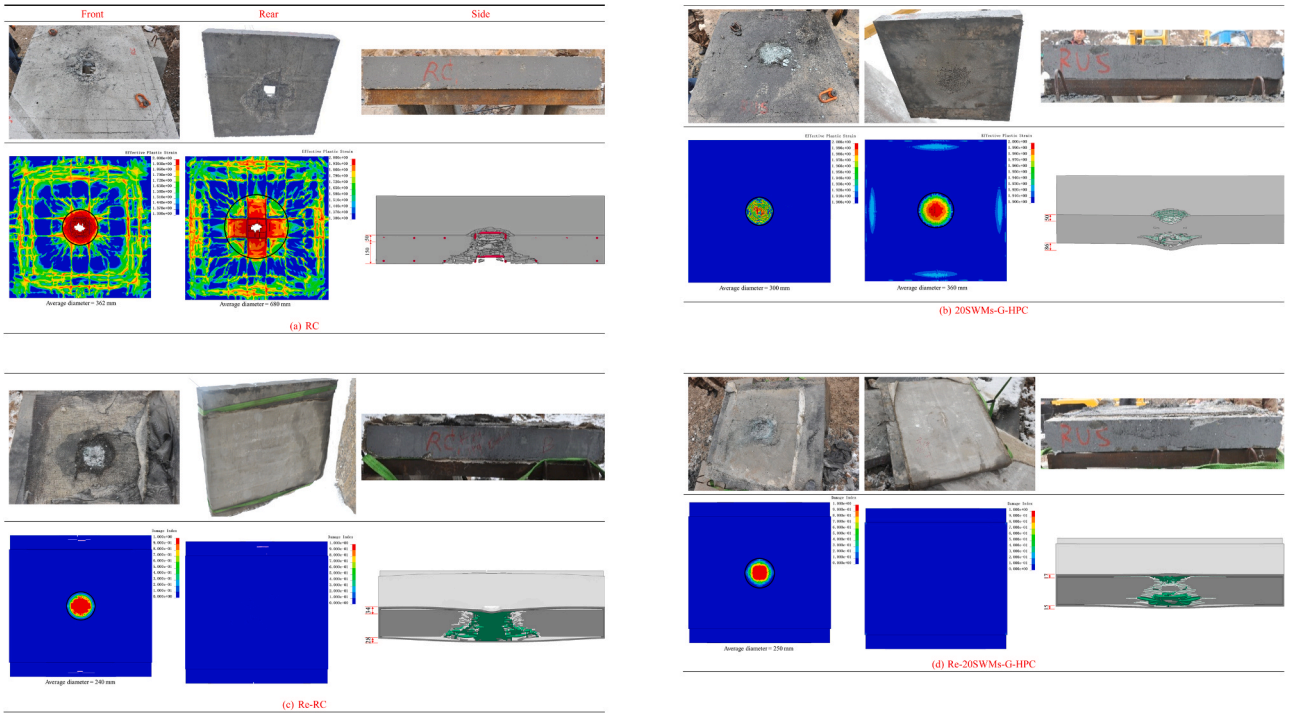

Fig. 9. Failure patterns of specimens subjected to contact detonations.

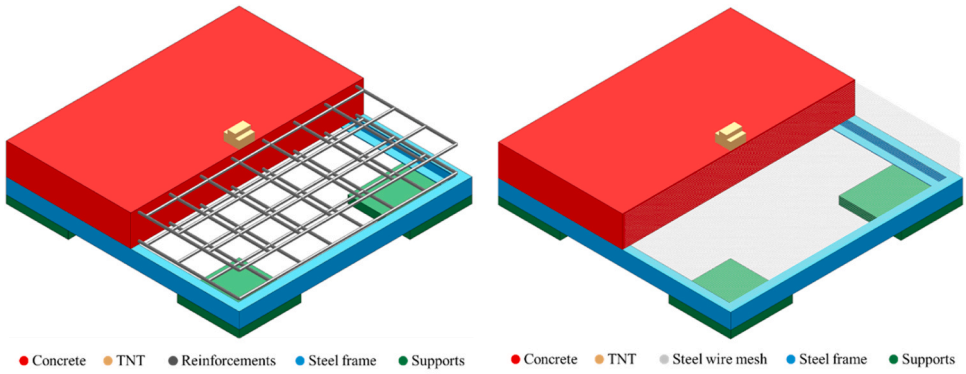

(a) RC model (b) 20SWMs-G-HPC model

Fig. 10. Details of RC and 20SWMs-G-HPC FE model.

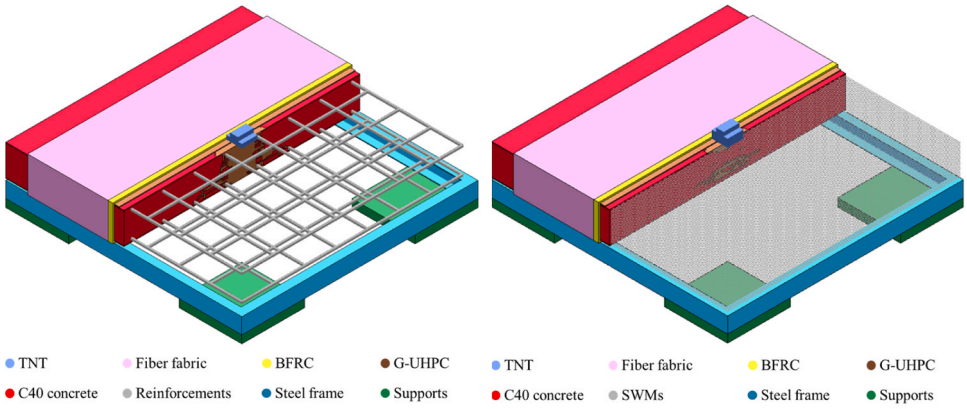

(a) Re-RC model (b) Re-20SWMs-G-HPC model

Fig. 11. Details of Re-RC and Re-20SWMs-G-HPC FE model.

(dynamic increase factor) is employed in this model to characterize the strain rate effect, as shown in Eq. (1).

$$DIF = 1 + \left(\frac{\dot{\varepsilon}}{C}\right)^{1/p} \tag{1}$$

in which, $C = 40$ and $p = 5$ as illustrated in literature [33].

6.2.2. Concrete material models

The supports are also treated as an elastic material and the concretes (C40 concrete, G-HPC and G-UHPC) were simulated by the K&C concrete material model. The yield strength surface ($\Delta\sigma_{yc}$), maximum strength surface ($\Delta\sigma_{mc}$), and residual strength surface ($\Delta\sigma_{rc}$) are employed in this model to describe the strength development of concrete under different stress states and paths, and the corresponding compressive meridians are shown in Eqs. (2) – (4). Three stress invariants (I_1, J_2, and J_3) are used to establish the current strength surface, and its relative is indicated by a function ($\eta(\lambda)$) of λ (modified effective plastic strain) in this model. The compressive meridians of the current strength surface are shown in Eqs. (5) and (6). The function $\eta(\lambda)$ is presented in the form of 13 (η, λ) pairs and users should manually input reasonable values for these pairs based on the experimental stress-strain relationship. Generally, this function begins with a value of 0 at $\lambda = 0$, then increases to 1 with λ increasing to λ_{max}, and eventually decreases back to 0 at a larger λ. More details on the explanation of the parameters in Eqs. (2) – (6) can be found in the literature [34–36], thus, no repetition was given here.

$$\Delta\sigma_{mc} = \begin{cases} a_0 + p/(a_1 + a_2 p), p \geq f_c^{'}/3 \\ (1.5/\psi)(p + f_t), \{0 \leq p \leq f_c^{'}/3\} or \{\lambda \leq \lambda_m \; and \; -f_t \leq p \leq f_c^{'}/3\} \\ 3(p/\eta + f_t), p \leq 0 \; and \; \lambda > \lambda_m \end{cases} \tag{2}$$

$$\Delta\sigma_{yc} = \begin{cases} a_{0y} + p\Big/(a_{1y} + a_{1y} p), p \geq f_{yc}^{'}\Big/3 \\ 1.35 f_t + 3p\left(1 - 1.35 f_t\Big/f_{yc}^{'}\right), 0 \leq p \leq f_{yc}^{'}\Big/3 \\ 1.35(p + f_t), p \leq 0 \end{cases} \tag{3}$$

$$\Delta\sigma_{rc} = a_{0r} + p/(a_{1r} + a_{2r} p) \tag{4}$$

$$\Delta\sigma = \eta(\lambda)\cdot(\Delta\sigma_{mc} - \Delta\sigma_{yc}) + \Delta\sigma_{yc} \tag{5}$$

$$\Delta\sigma = \eta(\lambda)\cdot(\Delta\sigma_{mc} - \Delta\sigma_{rc}) + \Delta\sigma_{rc} \tag{6}$$

Besides, this model has a function of auto-generating parameters based on the compressive strength of concrete. However, the auto-generated parameters can only well predict the mechanical behavior of concrete with the cubic strength range of 15 to 90 MPa, as demonstrated in the literature [37]. Therefore, the autogenerated values for the constants mainly including a_0, a_1, a_2 in $\Delta\sigma_{mc}$, a_{0y}, a_{1y}, a_{2y} in $\Delta\sigma_{yc}$, and a_{0r}, a_{1r}, a_{2r} in $\Delta\sigma_{rc}$ were exploited in this study.

Furthermore, the modified effective plastic strain λ determines the shear damage evolution of concrete in the K&C material model, as shown in Eq. (7):

$$\lambda = \begin{cases} \int_0^{\bar{\varepsilon}^p} \dfrac{d\bar{\varepsilon}^p}{r_f\left(1+p/r_f f_t\right)^{b_1}} & p \geq 0 \\ \int_0^{\bar{\varepsilon}^p} \dfrac{d\bar{\varepsilon}^p}{r_f\left(1+p/r_f f_t\right)^{b_2}} & p < 0 \end{cases} \tag{7}$$

in which, r_f refers to the DIF, b_1 and b_2 respectively represent the compressive and tensile damage scaling parameters that determine the speed of the descending branch of the stress-strain relationship under the uniaxial stress state. Notably, the modified effective plastic strain in the current form cannot describe the damage accumulation of concrete under the hydrostatic tensile stress state. With the increase in hydrostatic tensile stress, the pressure would reduce to its minimum -f_t, and keep it afterwards. Thus, a volumetric damage increment $\Delta\lambda$ was introduced into the deviatoric damage to overcome this shortcoming, as defined in Eq. (8).

$$\Delta\lambda = b_3 f_d k_d \left(\varepsilon_v - \varepsilon_{v,yield}\right) \tag{8}$$

$$f_d = \begin{cases} 1 - \left|\dfrac{\sqrt{3J_2}/p}{0.1}\right| & 0 \leq \sqrt{3J_2}/p < 0.1 \\ 0 & \sqrt{3J_2}/p \geq 0.1 \end{cases} \tag{9}$$

in which, b_3 is the damage scaling coefficient for the hydrostatic tensile state, k_d is an internal scalar multiplier, ε refers to the current volumetric strain, and $\varepsilon_{v,\ yield}$ is the volumetric strain when the material is at yielding. To evaluate the "closeness" of the current stress path to the triaxial tensile stress, the ratio $\left|\sqrt{3J_2/p}\right|$ is adopted in the K&C material model and f_d is a factor to limit the effect of this change, as shown in Eq. (9).

However, the damage accumulation of G-HPC is not the same as normal strength concrete (NSC) [10]. Hence, the auto-generated damage parameters are not suitable for geopolymer concrete and they should be modified based on the experimental data. The calibration process proposed in the literature [34] was exploited in this study to calibrate the above parameters for G-HPC. The details can be found in the literature [34]. After careful calibration, the parameters for predicting the mechanical behavior of G-HPC are shown in Table 7, and Fig. 12 indicates that the mechanical behavior of G-HPC under the uniaxial stress state could be well predicted by the K&C material model with the calibrated parameters.

The strain rate effect is critical for predicting the dynamic behavior of structural members under intense dynamic loading, especially the blast and impact loading, via numerical simulations. DIF is generally used to characterize the dynamic properties of concrete in the physical experiment, and it is also a convenient method to take the strain effect into a material in numerical simulation. Specifically, DIF is related to both strength enhancement and damage evolution of the concrete suffered from a high strain loading rate in the K&C model. Scholars found that the strain rate sensitivity of the G-HPC mortar was lower than that of normal-strength concrete [38,39]. Therefore, the empirical formulas proposed by Chen et.al [40] were employed to consider the strain rate effect of G-HPC in tension in the FE model in this study, as shown in Eq. (10). However, no DIF was introduced for compressive strength since it was concluded in the literature [41] that the increase in compressive strength of concrete at a high strain rate was caused by the structural effects, i.e., it was not a material property. Further, for the mesh objectivity of the local concrete material model, the "double-corrected" DIF to strain rate relationship proposed in the literature [41] was also exploited in this study. The details of the "double-corrected" DIF to strain rate relationship can be found in the literature [41], and repetition was given here.

It should be pointed out that the above-calibrated parameters were used for G-HPC, whereas the auto-generated parameters were used for C40 concrete. The parameters of the K&C model calibrated in the literature [34] were used for G-UHPC since its mechanical properties were similar to PC-UHPC as illustrated in the literature [10]. The HJC material model (MAT_JOHNSON_ HOLMQUIST_CONCRETE) was used for the BF-reinforced G-HPC used in the G-HPC canvas, and the parameters can be found in the literature [42], as listed in Table 8.

$$DIF_t = \begin{cases} 0.0805 \ln \dot{\varepsilon} + 1.9263 & 10^{-5} \leq \dot{\varepsilon} \leq 2.0\ s^{-1} \\ 1.5185 \ln \dot{\varepsilon} + 0.3465 & 2.0 \leq \dot{\varepsilon} \leq 20.0\ s^{-1} \end{cases} \tag{10}$$

6.3. Element type and erosion criteria

In the FE model, the air and TNT were regarded as fluid materials and simulated by the 1-point ALE multi-material element. The "structure" parts including concrete, steel frame, supports, and reinforcements were described by Lagrangian elements. Specifically, the constant stress solid element with a single-point integration was used to simulate the "structure" parts except for the reinforcements. The Hughes-Liu beam element was used to describe the behavior of reinforcements including steel bars and SWMs. It is worth noting that the "structure" parts were engulfed with the ALE domain, thus, the FSI between the slab and blast wave would be well performed.

To precisely predict the failure modes of the concrete slabs under the contact blast loading by numerical simulations and overcome possible computational difficulties generated from mesh distortion, the element erosion algorithm (MAT_ADD_EROSION) was employed in this study. The element erosion is not the physical material behavior, and there is no specific standard method for establishing failure criteria. Therefore, the repeat trial was adopted to establish suitable failure criteria in this study. A high degree of agreement was observed in the numerical results and the experimental data when the values assigned to the maximum principal strain and the maximum shear strain were 0.0475 and 0.28 for C40 concrete, and the values of the above parameters were set as 0.07 and 0.28 for G-HPC. Furthermore, due to the damage tolerance of G-UHPC was higher than G-HPC as indicated in Fig. 6, the maximum principal strain was set to be 0.1 for G-UHPC elements as illustrated in the literature [30]. A 0.2 effective plastic strain was used to reproduce the failure of SWMs, and no failure criteria were set for reinforcements since they were not fractured in the tests.

Table 7
Parameters of K&C material model for G-HPC (unit: kg, m, s).

a_0	a_1	a_2	b_1	b_2	b_3	l_c	ω
2.66e7	0.4463	8.978e-10	1.2	0.4	1.15	0.0065	0.75
a_{0y}	a_{1y}	a_{2y}	$a_{1\,f}$	$a_{2\,f}$	λ_1	λ_2	λ_3
7.812e6	0.625	7.35e-9	0.4417	3.38e-9	0	8.31013e-6	2.16149e-5
λ_4	λ_5	λ_6	λ_7	λ_8	λ_9	λ_{10}	λ_{11}
2.75005e-5	8.41e-5	2.7e-4	3.9e-4	6.1e-4	1e-3	1.65e-3	2e-3
λ_{12}	λ_{13}	η_1	η_2	η_3	η_4	η_5	η_6
1	100	0	0.85	0.95	0.98	1	0.4404
η_7	η_8	η_9	η_{10}	η_{11}	η_{12}	η_{13}	f_t
0.25938	0.09828	0.01759	0.001	0	0	0	4.24e6

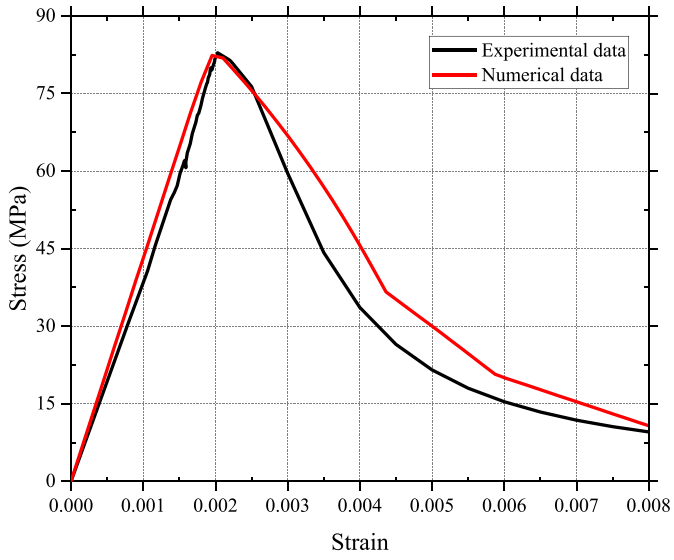

(a) Uniaxial compressive stress-strain relationship

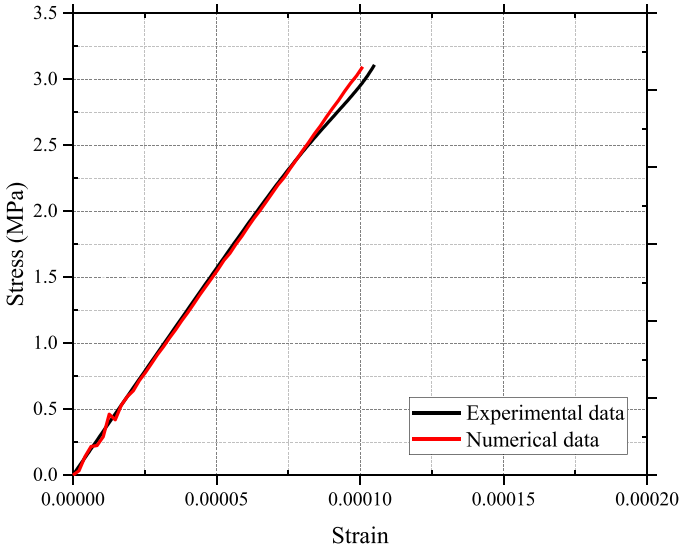

(b) Uniaxial tensile stress-strain relationship

Fig. 12. Comparison of test and simulation results of uniaxial stress-strain relationship.

Table 8
Parameters of HJC model for BF-reinforced G-HPC.

Parameter	Value	Parameter	Value	Parameter	Value
ρ (g/mm^3)	0.00237	T (MPa)	3.288	μ_{lock}	0.22
G (MPa)	11890	$\dot{\varepsilon}_s$	0.00001	D_1	0.04
A	0.47	$\varepsilon f_{\min}$	0.02	D_2	1
B	1.47	$S_{\max}$	7	K_1 (MPa)	85000
a	0.0567	P_{crush}(MPa)	9.033	K_2 (MPa)	-171000
b	0.258	μ_{crush}	0.00057	K_3(MPa)	208000
N	0.29	P_{lock}(MPa)	800	f_s	0
f_c (MPa)	32.46	I_f	0.136		

6.4. Validations

The failure modes and the dimensions of the crater or spalling/bulge observed in the numerical and experimental results were compared in Fig. 9 and Table 6. It was worth noting that the range of the effective plastic strain (damage index) to effectively describe the mostly damaged area should be determined by comparing the numerical and experimental results since there was no unified understanding on this topic [34,43]. It was found that, for the RC slab, the mostly damaged area described by the effective plastic strain (damage index) in the range of 1.3 to 2.0 could well agree with the crater and spalling observed in the experiments, whereas this range was converted to 1.9 to 2.0 for the

20SWMs-G-HPC slab since their damage tolerance is different. The damage index of the HJC model varied in the range of 0.0 to 1.0 was used to describe the damage of the rapidly repaired specimen with the UHMWPE woven fabric on the up surface of the specimen overturned in the experiments. The inner failures were also presented in this figure to illustrate the failure mode of the rapidly repaired specimen and compare the bulge size. Fig. 9 and Table 6 demonstrated that the developed FE models could precisely reproduce the failure modes observed in the tests. The dimensions of the crater, spalling, and bulge were also well-captured, especially the crater and spalling depths. It is worth noting that there is a slight difference between the simulation results and the experimental data. This discrepancy arises from the real-time effect of concrete damage on the strain rate effect, which might not have been fully considered in the finite element simulation.

Due to the reflection of the stress wave induced by the blast loading, coupled with the excellent mechanical properties of G-UHPC, the damaged G-HPC/C40 elements around the interface of G-HPC/C40 and G-UHPC were eroded. Moreover, for the specimen Re-RC, the G-UHPC used to repair the voids formed during the first explosion could keep its integrity, but the G-UHPC elements in the specimen Re-20SWMs-G-HPC presented obvious erosion. This demonstrated that the eroded G-HPC/C40 element dissipated the blast energy, therefore, protecting G-UHPC elements, but the protective effect was reduced after the adoption of the SWMs reinforcing the G-HPC. Meanwhile, debonding between the slab and the G-HPC canvas seemed to occur, which explained the overturn of the fiber fabric observed on the tests since the blast wave would enter the gap generated from the debonding. It reminds scholars that the bonding properties of the concrete canvas between the slab were worth more attention. Furthermore, it can be reasonably inferred from the numerical simulation that the G-HPC canvas on the rear surface mainly suffered from impact loading generated by the fragments with a high velocity, rather than blast loading since a significant debonding was observed between the G-HPC canvas and the internal slab on the rear surface.

6.5. Failure process

The failure mechanism of concrete or reinforced concrete slabs under contact blast loading has been well explained, as illustrated in the literature [44]. Thus, the progression of failure within the examined specimens Re-RC and Re-20SWMs-G-HPC are respectively presented in Fig. 13 and Fig. 14 to better understand the failure mechanism after rapidly repairing the specimen by G-UHPC and the proposed G-HPC canvas. Two display forms are exploited in Fig. 13 and Fig. 14, i.e., the left column exhibits the damage index propagation and the right column demonstrates the development of the element erosion. However, due to the disadvantage of the software LS-PREPOST, the deformation of the specimens was not shown in the display form of element erosion. In addition, the eroded elements simulating the repair material (G-UHPC) and the construction material of the slab (C40 or G-HPC) were illustrated in the display form of element erosion as purple and black elements, respectively.

Fig. 13 shows the failure process of the specimen Re-RC. It is notable that the damage development of the G-UHPC elements is indicated by the yellow circle in Fig. 13. The damage induced by the first blast was entrusted to the C40 concrete element at 0 ms, whereas the G-UHPC element (blue part in the middle area) did not present any damage. After the detonation of the charge (0.0015 ms), the G-UHPC elements were damaged and the crater was initially formed, however, the damage to C40 elements was not aggravated at the same time. When the blast wave persisted until 0.0045 ms, the damage to the G-UHPC elements was further aggravated and the C40 elements around the G-UHPC were

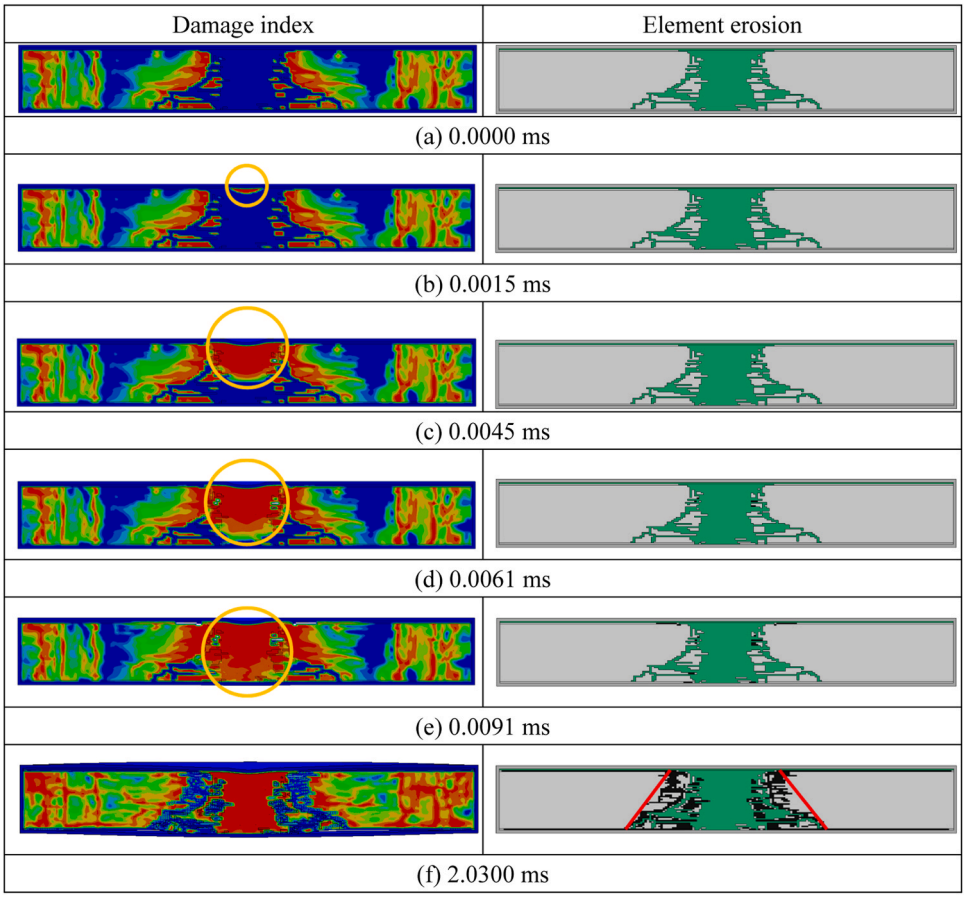

Fig. 13. Failure process of Re-RC slab.

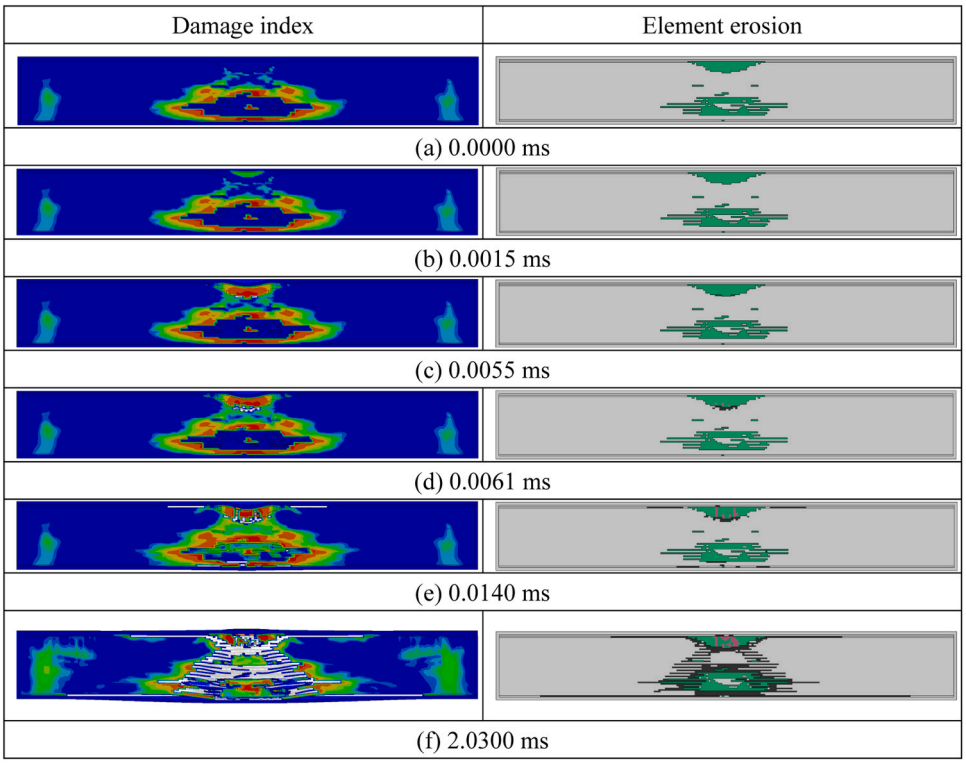

Fig. 14. Failure process of Re-20SWMs-G-HPC slab.

initially eroded (black elements). With the blast loading continuing, elements between the upper/rear G-HPC canvas and the internal slab were initially eroded (black elements) at 0.0061 ms and 0.0091 ms, respectively, indicating a debonding occurred, meanwhile, the damage to the G-UHPC was also aggregated. The erosion of the damaged C40 elements and the debonding continued until the specimen was destroyed (2.03 ms). Eventually, the internal slab of the Re-RC presented the punching failure mode since the C40 elements around G-UHPC were almost eroded and the outmost edge was almost in a straight line, as characterized by the red lines shown in Fig. 13(f).

The failure process of the specimen Re-20SWMs-G-HPC, revealed by the numerical simulations, is illustrated in Fig. 14. It indicated that the failure process of the specimen Re-20SWMs-G-HPC was similar to the specimen Re-RC when the blast wave persisted until 0.0061 ms. However, a new phenomenon was observed at 0.0061 ms, i.e., the G-UHPC elements filling the damaged area induced by the first blast event were initially eroded (purple elements). This may be generated from the reflected tensile stress on the surface between G-UHPC and G-HPC. Furthermore, the debonding between the rear G-HPC canvas and the internal slab was delayed to 0.014 ms. The processes including the damaged G-HPC elements erosion, G-UHPC element erosion, and the debonding continued until the specimen was destroyed (2.03 ms). Eventually, the internal slab of the Re-20SWMs-G-HPC presented the breach-perforation failure mode.

7. Parametric study

Based on the developed 3D FE model, a parametric study was conducted to investigate the effect of main parameters, such as the repair material, the thickness and location of the G-HPC canvas, and the steel-wire mesh, on the contact blast resistance of the rapidly repaired specimens, as shown in Table 9. The specimen Re-20SWMs-G-HPC was exploited as an example.

Fig. 15 shows the effect of repair materials filling the damaged area in the slab on the failure mode of the specimens. It indicates that repair materials have an insignificant effect on the distribution of the damage index shown in the left column of Fig. 15. However, the elements simulating the repair materials were more significantly eroded with the repair material changing to C40 from G-UHPC, as the development of the purple elements shown in the right column of Fig. 15. Meanwhile, the debonding area between the G-HPC canvas and the internal slab was also increased. Especially, the upper G-HPC canvas was almost completely deboned from the internal slab when C40 was used as the repair material since all the elements between the upper G-HPC canvas and the internal slab were almost eroded. Overall, all the internal slabs presented breach-perforation failure as indicated by the massive eroded G-HPC elements (black element), illustrating that the repair materials have an insignificant effect on the failure modes. However, it is believed

Table 9
Cases for parametric study.

Simulation cases	N_{swm}	Repair material	T_c (mm)	L_c	M_T (kg)
Re-20SWMs-G-HPC	20	G-UHPC	10	Top and bottom	1
1	20	G-HPC	10	Top and bottom	1
2	20	C40	10	Top and bottom	1
3	20	G-UHPC	20	Top and bottom	1
4	20	G-UHPC	30	Top and bottom	1
5	20	G-UHPC	10	Top	1
6	20	G-UHPC	10	Bottom	1
7	20	G-UHPC	10	No canvas	1
8	10	G-UHPC	10	Top and bottom	1
9	0	G-UHPC	10	Top and bottom	1

Note: In this table, N_{swm} refers to the number of layers of steel wire meshes; T_c refers to the thickness of the G-HPC canvas; L_c refers to the location of the G-HPC canvas; M_T refers to the mass of TNT.

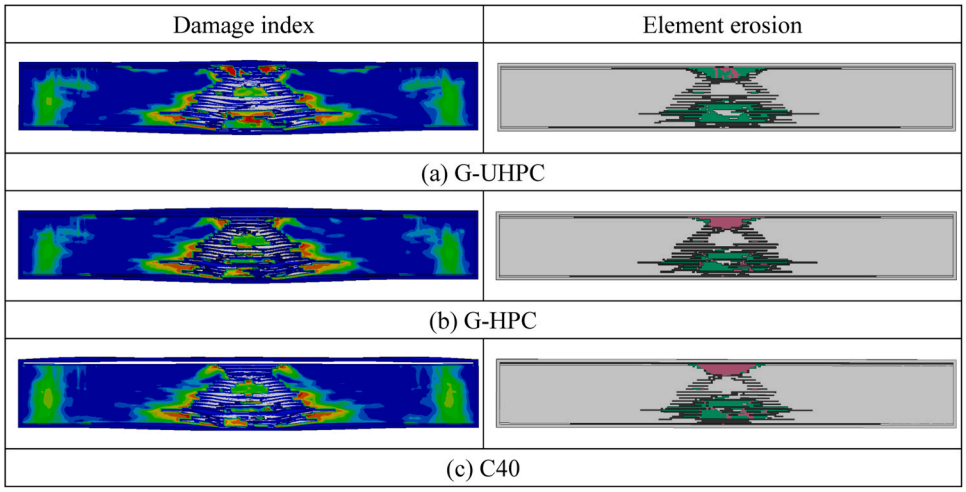

Fig. 15. Effect of repair materials filling the damaged area in the internal slab.

that the damage to the target induced by the fragments was significantly reduced by the adoption of the G-HPC canvas compared with the specimens without the canvas protection since the G-HPC canvas did not fail as shown in the numerical simulations. Interestingly, the area of the G-HPC elements erosion (black elements) in the internal slab seems to be decreasing with the reduction in mechanical properties of the repair material. This may be due to the failure of the G-HPC/C40 elements prior to the G-UHPC elements since an enormous gap exists in their mechanical properties, thereby dissipating the blast energy and protecting the G-UHPC elements.

Fig. 16 presents the influence of steel-wire mesh on the failure mode of the rapidly repaired specimens. Similarly, the steel-wire mesh has an insignificant effect on the distribution of the damage index, as shown in the left column of Fig. 16. The specimen with 10 layers of steel-wire mesh reinforcing or without steel-wire mesh reinforcing presented a punching failure since the outmost edges of the eroded G-UHPC (purple elements) and G-HPC (black elements) elements were almost in a straight line (red lines in Fig. 16(b) and Fig. 16(c)), whereas the specimen reinforced by 20 layers of SWMs showed the breach-perforation failure (Fig. 16(a)). Furthermore, the eroded elements of G-UHPC (purple elements) were significantly reduced when the SWMs increased from 10 layers to 20 layers, indicating that the increase in SWMs could reduce the damage to the G-UHPC filling the upper damaged area. Besides, the eroded element simulating the G-HPC (black elements) of the internal slab presented a larger distribution due to the interaction effect between SWMs and G-HPC when SWMs increase to 20 layers. In summary, the steel-wire mesh has a significant effect on the failure mode of rapidly repaired internal G-HPC slab, specifically, a lower damage level would be achieved by increasing the number of the steel-wire mesh.

Fig. 17 indicates that the location of the G-HPC canvas has a great effect on both the damage distribution and failure mode of the internal slab. Especially, the internal slab covered by the G-HPC canvas located on the upper surface presented a breach-perforation failure (Fig. 17(a)), whereas the punching failure was observed on the internal slab without the G-HPC canvas or covered at the bottom since the outermost edge of the eroded elements of G-HPC (black elements) and G-UHPC (purple elements) is almost in a straight line (red lines in Fig. 17(b) and Fig. 17(c)). Furthermore, the comparison of Fig. 17(c) and Fig. 9(b) indicates that the damage of the specimen rapidly repaired only by G-UHPC was much more severe than the specimen 20SWMs-G-HPC, demonstrating that it may not be feasible to repair the damaged specimen by G-UHPC only. When the G-HPC canvas was placed on the top surface, it could protect the G-UHPC elements, as illustrated by comparing Fig. 17(a) with Fig. 17(b) and Fig. 17(c). Moreover, the range of the element erosion of G-HPC (black elements) shown in Fig. 17 (b) and (c) was smaller than that shown in Fig. 17(a), indicating that the G-HPC canvas placed on the top surface could distribute the intense contact blast loading to a larger area. However, the damage to the important targets behind the slab induced by the fragments generated from the spalling of the rear concrete seems to be inevitable. This can be significantly

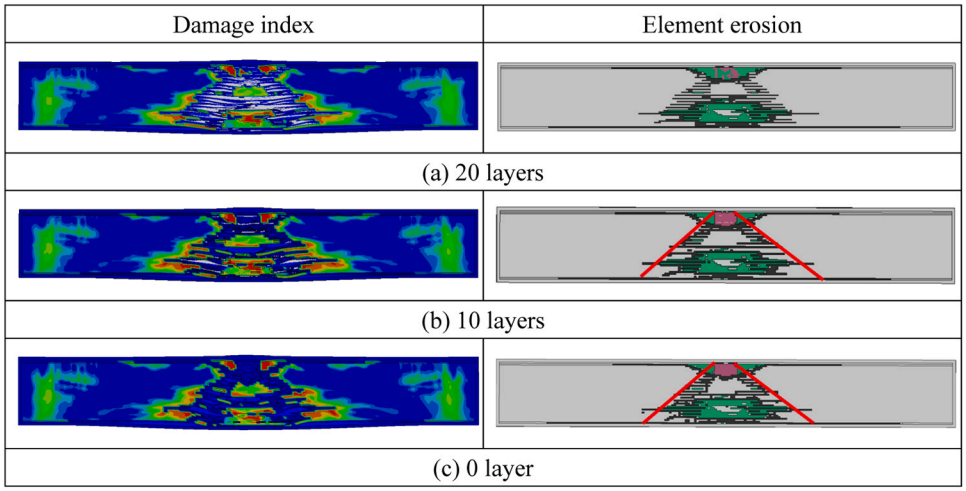

Fig. 16. Effect of steel-wire mesh.

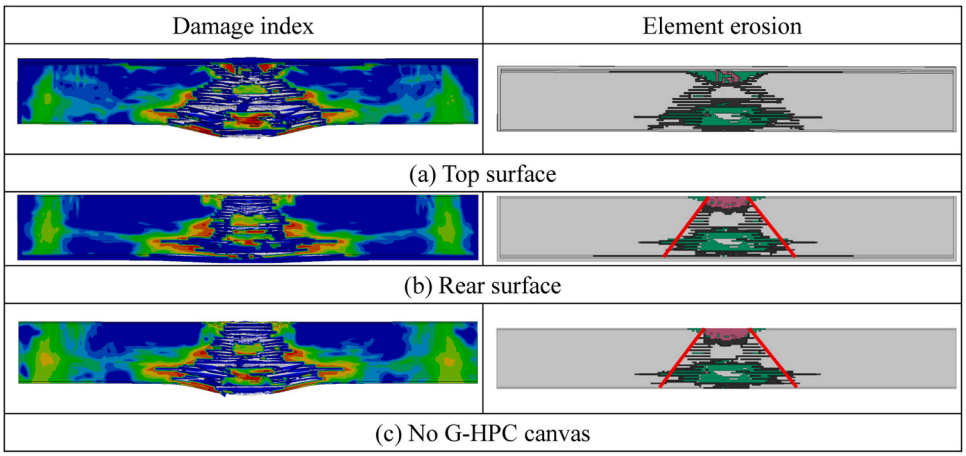

Fig. 17. Effect of G-HPC canvas location.

reduced by placing the canvas on the rear surface since the fragments would be caught in the canvas, as shown in Fig. 17 (b). From this perspective, it is more appropriate to place the G-HPC canvas on the rear surface.

Fig. 18 demonstrates the effect of the G-HPC canvas thickness. It indicates that the G-HPC canvas thickness has a remarkable influence on the damage index distribution. Meanwhile, all specimens presented a breach-perforation failure, but the element erosion area of G-UHPC (purple elements) and G-HPC (black elements) is significantly reduced with the canvas thickness increasing. It is reasonable to infer that the damage level would be further reduced with the increase in the G-HPC canvas thickness, even to transform the failure mode of the damaged internal slab. However, all specimens faced the debonding issue between the G-HPC canvas and the internal slab.

8. Conclusions

This study conducted contact blast tests to verify the feasibility of using the steel-wire mesh-reinforced G-HPC in pursuit of enhancing the blast resistance of the RC slab. A remedy method based on the G-HPC canvas and G-UHPC to rapidly repair the slabs damaged in the initial contact blast was proposed. The blast resistance of the rapidly repaired slabs was also investigated by the subsequent contact blast experiments. Eventually, numerical simulations were carried out to better understand the failure mechanism and the effect of main parameters including repair materials filling the internal slab, steel-wire mesh, G-HPC canvas location, and its thickness on the repaid repaired slabs. Based on the above study, the following conclusions can be drawn:

(1) The steel-wire mesh reinforced G-HPC slab had a superior blast resistance than the RC slab.
(2) The feasibility of the method using the G-HPC canvas and G-UHPC to rapidly repair the slab damaged in the first contact blast event was verified, whereas only using G-UHPC to fill the damage for the repair was not reasonable.
(3) The G-HPC canvas could remarkably decrease the dimensions of the crater on the post-explosion repaired slab and prevent spalling on the rear surface. Compared to its unrepaired condition, the diameter and depth of the crater of RC slab after repair have decreased by 45% and 30%, respectively, while the post-repair crater of 20SWMs-G-HPC slab exhibits a reduction of 30.7% in diameter and 75% in depth.
(4) For the rapidly repaired slab, the G-HPC canvas should be placed on the rear surface of the slab from the perspective of protecting the target behind the slab.
(5) Increasing the G-HPC canvas thickness and the layers of SWMs could significantly reduce the damage to the rapidly repaired slabs.

In future, it is recommended to explore improvements to the G-HPC canvas and G-UHPC repair methods, including variations in material composition and application techniques. Simultaneously, investigate the long-term durability of the repair method, considering factors such as environmental influences and aging. Optimize the placement of the G-

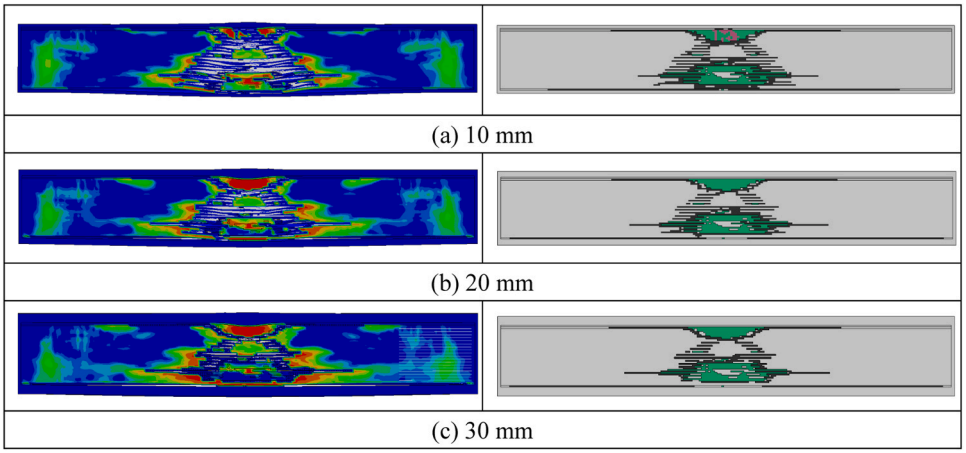

Fig. 18. Effect of G-HPC canvas thickness.

HPC canvas and integrate smart materials for real-time monitoring to validate the efficiency and effectiveness of the repair method under diverse real-world conditions.

CRediT authorship contribution statement

Ting Yang: Visualization, Software, Investigation. **Pengcheng Yuan:** Software, Methodology, Investigation, Data curation. **Jian Liu:** Software, Methodology, Investigation, Data curation. **Shenchun Xu:** Writing – original draft, Investigation, Conceptualization. **Hao Zeng:** Software, Investigation, Data curation. **Chengqing Wu:** Writing – review & editing, Supervision, Funding acquisition, Conceptualization. **Ruizhe Shao:** Visualization, Software. **Yu Su:** Validation, Software, Resources, Investigation.

Declaration of Competing Interest

We wish to confirm that there are no known conflicts of interest associated with this publication and there has been no significant financial support for this work that could have influenced its outcome.

Data availability

Data will be made available on request.

Acknowledgments

The research presented herein is jointly supported by the Guangdong Natural Science Foundation (Grant No. 2414070000926) and National Natural Science Foundation of China (Grant Nos. 51908155 and 51978186).

References

[1] Zhou Y, Xie YC, Pan T, Zhu W, Zhang H, Huang GY. Flexible materials and structures for mitigating combined blast and fragment loadings-a review. Int J Impact Eng 2023:104759.
[2] Yuan P, Xu S, Liu J, Su Y, Wu C. Experimental and numerical study of blast resistance of geopolymer based high performance concrete sandwich walls incorporated with metallic tube core. Eng Struct 2023;278:115505.
[3] Xu S, Wu P, Li Q, Zhou F, Chen B. Experimental investigation and numerical simulation on the blast resistance of reactive powder concrete subjected to blast by embedded explosive. Cem Concr Compos 2021;119:103989.
[4] Liao Q, Yu J, Xie X, Ye J, Jiang F. Experimental study of reinforced UHDC-UHPC panels under close-in blast loading. J Build Eng 2022;46:103498.
[5] Stewart MG, Li J. Risk-based assessment of blast-resistant design of ultra-high performance concrete columns. Struct Saf 2021;88:102030.
[6] Su Q, Wu H, Poh LH, Zhang F, Zhou F, Pang SD. Dynamic behavior of UHPC-FST under close-in explosions with large charge weight. Eng Struct 2023;277:115475.
[7] Das N, Nanthagopalan P. State-of-the-art review on ultra high performance concrete-Ballistic and blast perspective. Cem Concr Compos 2022;127:104383.
[8] Xu Z, Li J, Qian H, Wu C. Blast resistance of hybrid steel and polypropylene fibre reinforced ultra-high performance concrete after exposure to elevated temperatures. Compos Struct 2022;294:115771.
[9] Li J, Wu C, Hao H. Investigation of ultra-high performance concrete slab and normal strength concrete slab under contact explosion. Eng Struct 2015;102:395–408.
[10] Xu S, Yuan P, Liu J, Pan Z, Liu Z, Su Y, Li J, Wu C. Development and preliminary mix design of ultra-high-performance concrete based on geopolymer. Constr Build Mater 2021;308:125110.
[11] Davidovits J. High-alkali cements for 21st century concretes. Spec Publ 1994;144:383–98.
[12] Kathirvel P, Sreekumaran S. Sustainable development of ultra high performance concrete using geopolymer technology. J Build Eng 2021;39:102267.
[13] Karimipour A, de Brito J. Influence of polypropylene fibres and silica fume on the mechanical and fracture properties of ultra-high-performance geopolymer concrete. Constr Build Mater 2021;283(2021):122753.
[14] Nadi M, Allaoui D, Majdoubi H, Hamdane H, Haddaji Y, Mansouri S, Tamraoui Y, Manoun B, Hannache H, Oumam M. Effect of natural graphite additions on the microstructural and mechanical behavior of metakaolin based geopolymer materials. J Build Eng 2023:107562.
[15] Shee-Ween O, Cheng-Yong H, Yun-Ming L, Abdullah MMAB, Li-Ngee H, Pakawanit P, Khalid M, Muhammad S, H W, W B, Wan-En O, Yong-Jie H, Yong-Sing N, Hui-Teng N. Green development of fly ash geopolymer via casting and pressing approaches: strength, morphology, efflorescence and ecological properties. Constr Build Mater 2023;398:132446.
[16] Raza A, Alomayri T, Berradia M. Rapid repair of partially damaged GFRP-reinforced recycled aggregate concrete columns using FRP composites. Mech Adv Mater Struct 2022;29(27):6070–86.
[17] He R, Grelle S, Sneed LH, Belarbi A. Rapid repair of a severely damaged RC column having fractured bars using externally bonded CFRP. Compos Struct 2013;101:225–42.
[18] Hirde SK, Dudhal OS. Review on polymer modified concrete and its application to concrete structures. Int J Eng Res ISSN 2016;3:766–9.
[19] Faleschini F, Gonzalez-Libreros J, Zanini MA, Hofer L, Sneed L, Pellegrino C. Repair of severely-damaged RC exterior beam-column joints with FRP and FRCM composites. Compos Struct 2019;207:352–63.
[20] Raza A, Selmi A, El Ouni MH, Arshad M, Kahla NB. Rapid repair of geopolymer concrete members reinforced with polymer composites: parametric study and analytical modeling. Eng Struct 2024;299:117143.
[21] Wu RY, Pantelides CP. Rapid repair and replacement of earthquake-damaged concrete columns using plastic hinge relocation. Compos Struct 2017;180:467–83.
[22] Li Y, Wang J, Gao S, Zheng Y. Improvement effects of nano-silica on bonding performance of polymer concrete for repairing damaged concrete. Constr Build Mater 2023;409:133768.
[23] Ma X, Mei Z, Ma P. Influence of water to cement ratio on mechanical performance of concrete canvas reinforced with warp-knitted spacer fabric. Geotext Geomembr 2022;50(4):708–19.
[24] Zhang F, Chen H, Li X, Li H, Lv T, Zhang W, Yang Y. Experimental study of the mechanical behavior of FRP-reinforced concrete canvas panels. Compos Struct 2017;176:608–16.
[25] Xiang Z, Wang J, Niu J, Zhou J, Wang J. Experimental study on the mechanical properties of concrete canvas and CFRP jointly confined circular concrete columns under axial compression. Constr Build Mater 2023;385:130800.
[26] Zhang F, Chen H, Li X, Li H, Lv T, Zhang W, Yang Y. Experimental study of the mechanical behavior of FRP-reinforced concrete canvas panels. Compos Struct 2017;176:608–16.
[27] Han F, Chen H, Li X, Bao B, Lv T, Zhang W, Hui Duan W. Improvement of mechanical properties of concrete canvas by anhydrite-modified calcium sulfoaluminate cement. J Compos Mater 2016;50(14):1937–50.
[28] Han F, Chen H, Jiang K, Zhang W, Lv T, Yang Y. Influences of geometric patterns of 3D spacer fabric on tensile behavior of concrete canvas. Constr Build Mater 2014;65:620–9.
[29] Xu Shenchun, Yuan Pengcheng, Liu Jian, Yu Xiao, Hao Yifei, Hu Feng, Su Yu. Experimental and numerical investigation of G-UHPC based novel multi-layer protective slabs under contact explosions. *Eng Fail Analysis* 2022;142:106830.
[30] Liu J, Peng Y, Xu S, Yuan P, Qu K, Yu X, Hu F, Zhang W, Su Y. Investigation of geopolymer-based ultra-high performance concrete slabs against contact explosions. Constr Build Mater 2022;315:125727.
[31] GB50010–2010 (2010). Code for Design of Concrete Structures, Ministry of Housing and Urban-Rural Development of the People's Republic of China, Beijing, China.
[32] Chen, H. (2016). LS-DYNA structured ALE (S-ALE) solver. In Proceedings of the Fourteenth International LS-DYNA User Conference.
[33] Bao Yihai, Hai SLew, Sashi K. Kunnath. Modeling of reinforced concrete assemblies under column-removal scenario. J Struct Eng 2014;140(1):04013026.
[34] Xu Shenchun, Wu Pengtao, Wu Chengqing. Calibration of KCC concrete model for UHPC against low-velocity impact. Int J Impact Eng 2020;144:103648.
[35] Kong Xiangzhen, Fang Qin, Li QM, Wu Hao, John E. Crawford. Modified K&C model for cratering and scabbing of concrete slabs under projectile impact. Int J Impact Eng 2017;108:217–28.
[36] Malvar L, Javier John E, Crawford James WWesevich, Don Simons. A plasticity concrete material model for DYNA3D. Int J Impact Eng 1997;19(9-10):847–73.
[37] J.E. Crawford, Y. Wu, H.J. Choi, J.M. Magallanes, & S. Lan (2012). Use and validation of the release III K&C concrete material model in LS-DYNA, Karagozian & Case, Glendale.
[38] Khan MZN, Hao Y, Hao H, Shaikh FUA. Experimental evaluation of quasi-static and dynamic compressive properties of ambient-cured high-strength plain and fiber reinforced geopolymer composites. Constr Build Mater 2018;166:482–99.
[39] Liu K, Liu J, Li J, Tao M, Wu C. Experimental investigation of heating–cooling effects on the mechanical properties of geopolymer-based high performance concrete heated to elevated temperatures. Structures 2023;47:735–47.
[40] Chen C, Zhang X, Hao H. Dynamic tensile properties of geopolymer concrete and fibre reinforced geopolymer concrete. Constr Build Mater 2023;393:132159.
[41] Li XQ, Chen QJ, Chen JF, Liao JZ, Lu Y. Dynamic increase factor (DIF) for concrete in compression and tension in FE modeling with a local concrete model. Int J Impact Eng 2022;163:104079.
[42] Xie L, Sun X, Yu Z, Guan Z, Long A, Lian H, Lian Y. Experimental study and theoretical analysis on dynamic mechanical properties of basalt fiber reinforced concrete. J Build Eng 2022;62:105334.
[43] Cui J, Guan X, Shi Y, Li Z. A high-fidelity constitutive model considering hydrostatic damage for predictions of high dynamic properties of concrete structures. Comput Struct 2023;287:107115.
[44] Zhang C, Gholipour G, Mousavi AA. Blast loads induced responses of RC structural members: state-of-the-art review. Compos Part B: Eng 2020;195:108066.